Title

Relative Patlak plot for dynamic PET parametric imaging without the need for early-time input function

Journal

Physics in Medicine and Biology, 63(16)

ISSN

0031-9155

Authors

Zuo, Yang
Qi, Jinyi
Wang, Guobao

Publication Date

2018-08-01

DOI

10.1088/1361-6560/aad444

Peer reviewed

HHS Public Access

Author manuscript

Phys Med Biol. Author manuscript; available in PMC 2019 August 10.

Published in final edited form as:

Phys Med Biol. ; 63(16): 165004. doi:10.1088/1361-6560/aad444.

Relative Patlak Plot for Dynamic PET Parametric Imaging Without the Need for Early-time Input Function

Yang Zuo[1], **Jinyi Qi**[2], and **Guobao Wang**[1,3]

[1]Department of Radiology, University of California at Davis

[2]Department of Biomedical Engineering, University of California at Davis

[3]Comprehensive Cancer Center, University of California at Davis

Abstract

The Patlak graphical method is widely used in parametric imaging for modeling irreversible radiotracer kinetics in dynamic PET. The net influx rate of radiotracer can be determined from the slope of the Patlak plot. The implementation of the standard Patlak method requires the knowledge of full-time input function from the injection time until the scan end time, which presents a challenge for use in the clinic. This paper proposes a new relative Patlak plot method that does not require early-time input function and therefore can be more efficient for parametric imaging. Theoretical analysis proves that the effect of early-time input function is a constant scaling factor on the Patlak slope estimation. Thus, the parametric image of the slope of the relative Patlak plot is related to the parametric image of standard Patlak slope by a global scaling factor. This theoretical finding has been further demonstrated by computer simulation and real patient data. The study indicates that parametric imaging of the relative Patlak slope can be used as a substitute of parametric imaging of standard Patlak slope for tasks that do not require absolute quantification, such as lesion detection and tumor volume segmentation.

1. Introduction

Dynamic positron emission tomography (PET) provides four-dimensional distribution (three-dimensional space plus one-dimentional time) of radiotracer in living body and is attracting more and more research interests [Schmidt and Turkheimer, 2002, Rahmim et al, 2009, Wang and Qi, 2013, Reader and Verhaeghe, 2014]. Analyzing dynamic PET data relies on kinetic modeling which commonly uses a temporal model to describe the kinetics of radiotracer uptake [Schmidt and Turkheimer, 2002]. Voxel-wise implementation of kinetic modeling provides parametric maps of kinetic parameters indicating the biological characters of the tissue [Gunn et al., 1998]. Parametric imaging has been found useful in many applications including tumor detection [Kordower et al., 2000, Gill et al., 2003] and extraction of metabolic tumor volume (MTV) [Visser et al., 2008].

The Patlak graphical plot is a widely used kinetic analysis method in dynamic PET for extracting the net influx rate of irreversible uptake of a radiotracer [Patlak et al., 1983, Patlak and Blasberg, 1985]. It is also used for kinetic modeling in dynamic magnetic resonance imaging (MRI) [Hackstein et al., 2003] and computed tomography (CT) [Hackstein et al., 2004, Miles et al., 1999, Hom et al., 2009]. Compared with nonlinear compartmental

modeling, the Patlak method uses a linear model and has the advantage of being computationally efficient for parametric imaging and being easier to be implemented into new reconstruction methods [Wang et al., 2008, Tsoumpas et al., 2008, Tang et al., 2010, Angelis et al., 2011, Zhu et al., 2013] and for whole-body imaging [Karakatsanis et al., 2015, Karakatsanis et al., 2016, Zhu et al., 2013, Hu et al., 2017].

Input function is essential for tracer kinetic modeling. Although the Patlak graphical plot only examines the time points of tissue activity at steady state, the standard Patlak method requires the knowledge of full-time input function from the radiotracer injection time until the dynamic scan end time. To obtain the information of full-time input function, either many blood samples are needed if arterial blood sampling is used or a long scan covering early-time points is required if the image-derived or reference region input function is used. For example in dynamic ^{18}F-FDG PET imaging, an one-hour dynamic scan is required to derive the full blood input function from dynamic images, though only late 20–30 minutes are actually used to extract the tracer activity of tissue. This requirement for early-time input function presents a challenge for applying the Patlak method in the clinic, particularly for whole-body imaging [Hu et al., 2017].

This paper proposes a new relative Patlak plot method for PET parametric imaging. Compared with the standard Patlak plot, the proposed relative plot does not require the information of early-time input function. Mathematical analysis is used to show the relationship between the slope of the new plot and that of the standard Patlak plot. The theoretical findings are further validated by computer simulation of dynamic PET data and real patient scan data.

2. Theory

2.1. Standard Patlak Plot

Let us denote the radiotracer concentration at time t in a tissue region of interest (ROI) or voxel by $C_T(t)$ and tracer concentration in the plasma by $C_P(t)$. The Patlak plot exploits the linearity between the normalized tissue concentration and normalized integral of input function $C_P(t)$ after a steady-state time t^* Mathematically, it is described by a linear equation:

$$\frac{C_T(t)}{C_P(t)} = K_i \cdot \frac{\int_0^t C_P(\tau)d\tau}{C_P(t)} + b\left(t > t^*\right), \quad (1)$$

where K_i is the slope constant that represents the net influx rate of irreversible uptake of a radiotracer and b is the intercept which equivalently indicates blood volume in the tissue and the normalized tracer concentration from reversible compartments.

By acquiring dynamic PET data for multiple time frames, one can plot the data of

$$y(t) = \frac{C_T(t)}{C_P(t)} \quad (2)$$

and

$$x(t) = \frac{\int_0^t C_P(\tau)d\tau}{C_P(t)} \quad (3)$$

of each time frame and fit the data points using the linear model Eq. (1). The slope K_i and intercept b are then estimated by the linear regression. Note that although $y(t)$ is only sampled for $t > t^*$, $x(t)$ contains the integral of the input function $C_P(t)$ from the injection time $t = 0$ till the scan end time. Thus the full-time input function needs to be known for the standard Patlak plot.

Given a set of measurements at M time points $\{t_m\}_{m=1}^{M}$ with $t = t^*$ and t_m denoting the midpoint of each time frame, the Patlak slope and intercept can be estimated using the following least-squares formulation,

$$\hat{K}_i, \hat{b} = \underset{K_i, b}{\operatorname{argmin}} \sum_{m=1}^{M} \left[y(t_m) - K_i \cdot x(t_m) - b \right]^2. \quad (4)$$

where the integration in $x(t)$ is calculated using the rectangle rule,

$$x(t_m) = \frac{\sum_{n=1}^{m} C_P(t_n) \Delta t_n}{C_P(t_m)},$$

with Δt_n denoting the scan duration for nth frame. The optimal solution has the following analytic formula

$$\hat{K}_i = \frac{V(x, y)}{V(x, x)}, \quad (5)$$

$$\hat{b} = \bar{y} - \hat{K}_i \cdot \bar{x}, \quad (6)$$

where $V(\cdot, \cdot)$ and $\bar{\cdot}$ have the forms as follows

$$\bar{x} = \frac{1}{M}\sum_{m=1}^{M} x(t_m), \quad (7)$$

$$V(x,y) = \frac{1}{M}\sum_{m=1}^{M} x(t_m)y(t_m) - \bar{x}\cdot\bar{y}, \quad (8)$$

which correspond to the mean and covariance if x and y are considered as random variables.

2.2. Proposed Relative Patlak Plot

We propose a new relative Patlak plot which has the following model equation:

$$\frac{C_T(t)}{C_P(t)} = K'_i \cdot \frac{\int_{t^*}^{t} C_P(\tau)d\tau}{C_P(t)} + b'(t > t^*), \quad (9)$$

where $\hat{K}'_i$ and b' are the slope and intercept of the new plot, respectively.

The new relative Patlak method plots the data of $y(t)$ in Eq. (2) versus

$$x'(t) = \frac{\int_{t^*}^{t} C_P(\tau)d\tau}{C_P(t)} \quad (10)$$

to get the slope $\hat{K}'_i$ and intercept b'. This new model is very similar to the standard Patlak plot equation, except that the integral of the input function $C_P(t)$ here is from t^* to t, not from 0 to t. The integral of $C_P(t)$ over early time from 0 to t^* is no longer needed in this new plot.

Similarly to the least-squares estimation for the standard Patlak plot, the slope and intercept of the relative Patlak plot can be estimated by

$$\hat{K}'_i, \hat{b}' = \arg\min_{K'_i, b'} \sum_{m=1}^{M} \left[y(t_m) - K'_i \cdot x'(t_m) - b'\right]^2, \quad (11)$$

which gives the following optimal solution

$$\widehat{K'}_i = \frac{V(x', y)}{V(x', y')}, \quad (12)$$

$$\hat{b}' = \bar{y} - \widehat{K'}_i \cdot \bar{x}'. \quad (13)$$

where $\bar{\cdot}$ and $V(\cdot, \cdot)$ are defined in Eqs. (7) and (8), respectively.

2.3. Theoretical Relation Between the Two Plots

The new relative Patlak plot is closely related to the standard Patlak plot. Here we examine the theoretical relation between the two plots using analytical derivations. Let us define

$$x^0(t) = \frac{\int_0^{t^*} C_P(\tau) d\tau}{C_P(t)} \quad (14)$$

to account for the component of early-time input function which appears in $x(t)$ but not in $x'(t)$. Obviously, we have

$$x(t) = x^0(t) + x'(t). \quad (15)$$

In dynamic PET scans, the late-time input function $C_P(t)$ for $t > t^*$ can be analytically expressed by an exponential function:

$$C_P(t) = a_1 \cdot e^{-a2t}, \quad (16)$$

where a_1, $a_2 > 0$. For example, the widely used Feng model for dynamic ^{18}F-FDG PET has the form [Feng et al., 1993]

$$C_P(t) = (A_1 t - A_2 - A_3) e^{-L_1 t} + A_2 e^{-L_2 t} + A_3 e^{-L_3 t}, \quad (17)$$

with the following parameters A_1 = 851.1 mg/100mL/min, A_2 = 21.9 mg/100mL, A_3 = 20.8 mg/100mL, L_1 = 4.1 min^{-1}, L_2 = 0.12 min^{-1}, L_3 = 0.01 min^{-1}. For $t > t^*$ = 30 minutes, the Feng input function is dominated by the term $A_3 e^{-L3t}$ while the other two terms are negligible. Another example is the reference tissue input in dynamic ^{11}C-PIB PET, where the tail also approximately follows an exponential function [Zhou et al., 2012].

As a result, $x^0(t)$ and $x'(t)$ can be rewritten as

$$x^0(t) = \frac{s^*}{a_1} e^{a_2 t}, \quad (18)$$

$$x'(t) = \frac{1}{a_2}\left(e^{-a_2(t^* - t)} - 1\right), \quad (19)$$

with s^* being the integral of blood input over the early time from time 0 to t^*,

$$s^* = \int_0^{t^*} C_P(\tau) d\tau . \quad (20)$$

It is then not difficult to verify the following linear relationship between $x^0(t)$ and $x'(t)$:

$$x^0(t) = \alpha + \beta x'(t) \quad (21)$$

where α and β are both constants that only depend on t^*:

$$\alpha = \frac{1}{a_1} s^* e^{a_2 t^*}, \quad (22)$$

$$\beta = \frac{a_2}{a_1} s^* e^{a_2 t^*} . \quad (23)$$

Using Eq. (15), the standard Patlak plot model Eq. (1) can be re-written as

$$y(t) = K_i \cdot \left[x'(t) + x^0(t)\right] + b . \quad (24)$$

Substituting Eq. (21) into Eq. (24), we obtain the following equivalence,

$$y(t) = (1 + \beta) K_i \cdot x'(t) + \left(\alpha K_i + b\right), \quad (25)$$

$$= K'_i x'(t) + b' \quad (26)$$

With

$$K'_i = (1 + \beta)K_i, \quad (27)$$

$$b' = b + \alpha K_i. \quad (28)$$

The two equations above indicate that the relative Patlak slope K'_i is proportional to the standard Patlak slope K_i with a scaling factor $(1 + \beta)$. The intercept of the relative Patlak plot is equivalent to the intercept of the standard Patlak plot plus a shift αK_i.

The scaling factor $(1 + \beta)$ only depends on the input function and is independent of tissue time activity. It is therefore a global scaling factor when the Patlak plot is implemented for parametric imaging. Thus, the parametric image of the relative Patlak slope K'_i is equivalent to the parametric image of the standard Patlak slope K_i up to a scaling factor.

2.4. Theoretical Relation Between the Least Squares Estimates

In practice, the slope and intercept of a graphical plot are commonly estimated by a least squares optimization. Here we examine the theoretical relation between the standard Patlak and relative Patlak least squares estimates.

Based on Eq. (21), $x(t)$ and $x'(t)$ approximately satisfy a linear relation:

$$x(t) = \nu + S \cdot x'(t) \, (t > t^*), \quad (29)$$

where S and ν are respectively equivalent to $(1 + \beta)$ and α if the late-time blood input is described by an exponential function. Alternatively, S and ν can be estimated by a linear regression without assuming an exponential model:

$$S = \frac{V(x', x)}{V(x', x')}, \quad (30)$$

$$\nu = \bar{x} - S \cdot \bar{x}'. \quad (31)$$

Substituting Eq. (29) into the least squares estimate of the standard Patlak slope $\widehat{K}_i$ in Eq. (5) leads to the following expression,

$$\widehat{K}_i = \frac{V(\nu + Sx', y)}{V(\nu + Sx', \nu + Sx')}. \quad (32)$$

Note that the function $V(\cdot, \cdot)$ has the following properties:

$$V(x, y) = V(y, x), \quad (33)$$

$$V(c \cdot x, y) = c \cdot V(x, y), \quad (34)$$

$$V(c + c, y) = V(x, y), \quad (35)$$

where c is an arbitrary constant. Using these properties and the definition of the least-squares estimate of the relative Patlak slope K'_i defined in Eq. (12), we then obtain the scaling relation between K'_i and K'_i:

$$\widehat{K}'_i = S \cdot \widehat{K}_i. \quad (36)$$

We can also derive the following relation between the least-squares estimates of the two intercepts $\hat{b}'$ and $\hat{b}$:

$$\hat{b}' = \hat{b} + \nu \cdot \widehat{K}_i. \quad (37)$$

These results indicate that the theoretical relation between the standard Patlak plot and relative Patlak plot holds true as long as $x(t)$ and $x'(t)$ satisfy the linear relationship given in Eq. (29) regardless of the shape of the blood input function.

3. Materials and Methods

3.1. Validation Using Computer Simulation

We first conducted a computer simulation to validate the theoretical results on the scaling relationship between the standard Patlak slope and relative Patlak slope. This simulation study was designed for mimicking parametric imaging where a single blood input function is used and different voxels share the same scaling factor between the standard Patlak slope and relative Patlak slope. One-hour dynamic ^{18}F-FDG scan was simulated following the scanning sequence of a total of 55 frames: 30 × 10-second frames, 10 × 60-second frames and 15 × 180 -second frames. The blood input function in this simulation was generated using the analytical Feng model [Feng et al., 1993]. Following the standard two-tissue compartmental model, we simulated 10; 000 groups of random kinetic parameters which follow a Gaussian distribution with the mean of kinetic parameters being K_1 = 0.81 mL/mL/min, k_2 = 0.38 min^{-1}, k_3 = 0.1 min^{-1}, k_4 = 0 min^{-1} and standard deviation being 40% of the mean kinetic parameters. Noise-free time activity curves (TACs) were generated with the simulated FDG kinetics and blood input function. Zero-mean Gaussian noise were then

added to each noise-free TAC $\{c_m\}_{m+1}^{M}$ using the noise standard deviation [Wu and Carson, 2002] defined by

$$SD_m = S_c \cdot \sqrt{c_m \exp(\lambda t_m) / \Delta t_m}, \quad (38)$$

where S_c is a scale factor to adjust SD to match with realistic dynamic FDG-PET data at different noise levels. $S_c = 1.0$ was used to simulate a voxel-level high noise in this simulation. λ is the decay constant of the radiotracer set to be $\ln(2)/T_{1/2}$ with $T_{1/2} = 109.8$ minutes. Δt_m is the scan duration of time frame m and t_m is the middle time of frame m.

To demonstrate the wide applicability of the method, we conducted a second simulation study to examine if a bi-exponential input model $C_P(t) = a_1 e^{-a_2 t} + b_1 e^{-b_2 t}$ meets the linear relation between $x(t)$ and $x'(t)$. The scanning sequence was the same as used in the first simulation study. To mimic blood input functions of different tail shape, one thousand sets of the model parameters were randomly generated using the uniform distribution with the intervals $a_1 \in [0, 50]$, $b_1 \in [0, 50]$, $a_2 \in [0, 1]$, $b_2 \in [0, 1]$. The parameter bounds are projected from the Feng input model. The coefficient of the Pearson correlation between $x(t)$ and $x'(t)$ was calculated for each realization of the input function.

3.2. Validation Using Patient Scans

We further validated the theoretical results using dynamic FDG-PET scans of two human patients, one with breast cancer and the other with coronary heart disease.

The breast patient scan was operated on the GE Discovery 690 PET/CT scanner at UC Davis Medical Center. The patient received 5 mCi ^{18}F-FDG with a bolus injection. List-mode time-of-flight data acquisition commenced right after the FDG injection and lasted for 60 minutes. A low-dose transmission CT scan was then performed at the end of PET scan to provide CT image for PET attenuation correction. The raw data were then binned into a total of 49 dynamic frames: 30 × 10 seconds, 10 × 60 seconds and 9 × 300 seconds. Dynamic PET images were reconstructed using the standard ordered subsets expectation maximization (OSEM) algorithm with 2 iterations and 32 subsets as provided in the vendor software. All data corrections including normalization, attenuation correction, scattered correction and randoms correction, were included in the reconstruction process. A region of interest was placed in the left ventricle region to extract blood input function.

The cardiac scan was performed on the GE Discovery ST PET/CT scanner at UC Davis Medical Center in two-dimensional mode. The scanner has no time-of-flight capability. The patient received 20 mCi ^{18}F-FDG with a bolus injection. List-mode data acquisition commenced right after the FDG injection and lasted for 60 minutes. A low-dose transmission CT scan was then performed at the end of PET scan to provide CT image for PET attenuation correction. The raw data were binned into a total of 49 dynamic frames: 30 × 10 seconds, 10 × 60 seconds and 9 × 300 seconds. Dynamic PET images were reconstructed using the standard ordered subsets expectation maximization (OSEM)

algorithm with 2 iterations and 30 subsets as provided in the vendor software. All data corrections including normalization, attenuation correction, scattered correction and randoms correction, were included in the reconstruction process. The blood input function was also extracted from the left ventricle region.

4. Results

4.1. Simulation Results

The simulated noisy TACs based on the Feng input model were first analyzed using the standard Patlak plot and new relative Patlak plot with a start time $t^* = 30$ minutes. For the standard Patlak plot, the full-time blood input from 0 to 60 minutes was used to estimate the slope K_i. For the relative Patlak plot, only the input function after t^* was used to estimate the slope K'_i. Early-time input function is not needed for the relative Patlak plot, which is equivalent to setting those time points to zeros. The two input functions are graphically compared in Fig. 1(a). We then verified the linear relation between $\left(\int_0^t C_P(\tau)d\tau\right) / C_P(t)$ and $x'(t) = \left(\int_{t^*}^t C_P(\tau)d\tau\right) / C_P(t)$ with $t > t^*$. Figure 1(b) shows the plot of $x(t)$ versus $x'(t)$ for the simulated Feng input function. The linear fit was excellent with a pairwise linear correlation coefficient close to 1.

Examples of the the standard Patlak plot and relative Patlak plot are shown in Fig. 2(a) and (b). We examined the linearity between the standard Patlak slope K_i and the relative Patlak slope K'_i. Fig. 3(a) shows the estimated K'_i versus K_i values for all the simulated 10, 000 TACs. The correlation coefficient between K'_i and K_i was 1.0, indicating a perfect linearity. The intercept is negligible, indicating K'_i values are equal to K_i values times the scaling factor. The slope of the linear plot of K'_i versus K_i is approximately equal to the slope of the linear plot of $x(t)$ versus $x'(t)$. The relation between K'_i and K_i is therefore verified by the simulation data. Fig. 3(b) further shows that the correlation coefficient between K'_i and K_i remains stable and close to 1 when t^* varied from 10 minutes to 54 minutes, though the scaling factor between them depends on t^*. Note that t^* could not be greater than 54 minutes given the defined time frames, otherwise less than two time points could be used for the Patlak plots.

Fig. 4(a) shows all the correlation coefficients of $x'(t)$ versus $x(t)$ for 1,000 random realizations of the bio-exponential input function. Fig. 4(b) show the correlation plot of $x'(t)$ versus $x(t)$ for a specific model parameter set $a_1 = 36.288$, $a_2 = 0.093$, $b_1 = 1.543$, $b_2 = 0.001$, which corresponds to the the sample point in Fig. 4(a) with the lowest correlation coefficient $R = 0.9927$. The results validate the wide applicability of the assumption [Eq. (29)] we made for establishing the relation between the relative Patlak slope and standard Patlak slope.

4.2. Patient Results

4.2.1. Blood Input Functions—The image-derived input functions from the breast patient scan and cardiac patient scan are shown in Fig. 5(a) and Fig. 5(b), respectively. The start time t^* was initially set to 30 minutes. Fig. 6 validates that the late-time time points of the two blood input functions approximately follow a mono-exponential model $C_P(t) = a_1 e^{-a2t}$ for $t \geq t^*$. It is not surprising that higher noise presents in the cardiac patient data because the scan was operated in a 2D mode and also without time-of-flight capability.

The linear relation between $x(t)$ and $x'(t)$ after $t^* = 30$ minutes is shown in Fig. 7(a) for the breast patient data and in Fig. 7(b) for the cardiac patient data.

4.2.2. Breast Patient Result—The parametric maps of K_i by the standard Patlak model and K'_i by the relative Patlak model with $t^* = 30$ minutes are shown in Fig. 8 for transverse, sagittal and coronal planes. The standardized uptake value (SUV) images by the static scan at 55–60 minutes are also included for a comparison with parametric imaging. The two parametric images have different absolute values but they appear to be proportional to each other. Compared with the SUV images, the K_i and K'_i images demonstrated higher contrast in the breast tumor region.

The plot of K'_i versus K_i is shown in Fig. 9(a). It is clear that K'_i was linearly related to K_i with a slope of 1.6199 and intercept of 1.7345×10^{-7}. The intercept was negligible so the linear relation was simply a scaling. The slope of the linear plot of K'_i versus K_i is very close to the slope of the linear plot of $x(t)$ versus $x'(t)$. The correlation coefficients between K'_i and K_i was close to 1. Fig. 9(b) further shows the correlation coefficient between K'_i and K_i versus various t^* values ranging from 10 minutes to 50 minutes. High correlation remains between K'_i and K_i.

4.2.3. Cardiac Patient Result—The SUV images of the last frame (55–60 minutes), parametric maps of K_i by the standard Patlak model and K'_i by the relative Patlak model with $t^* = 30$ minutes are shown in Fig. 10. Again, the two parametric images appear to be proportional to each other, though with different absolute values. The contrast of the myocardim over the blood pool is higher in the parametric images than in the SUV images.

The plot of K'_i versus K_i is shown in Fig. 11(a). It is again clear that K'_i is linearly related to K_i with a slope of 1.2898 and intercept of 7.7×10^{-6}. The negligible intercept indicates that the linear relation is a scaling. The slope between K'_i versus K_i is very close to the slope between $x(t)$ versus $x'(t)$ shown in Fig. 7(b). The correlation coefficients between K'_i and K_i and between $x(t)$ and $x'(t)$ are close to 1.

The correlation coefficient between K'_i and K_i is further plotted versus the start time t^* in Fig. 11(b). The correlation coefficient values remain above 0.90, though the one at $t^* = 45$ minutes is slightly lower then others. This can be explained by the fact in Fig. 7(b) that the

linear correlation between x and x' for t^* = 45 minutes (i.e., the last three points) is relatively weaker, possibly due to higher noise in the cardiac scan. The corresponding K_i and K'_i images for t^* = 45 minutes are shown in Fig. 12. Overall, the two images still have very similar contrast appearance, indicating the scaling relation between K_i and K'_i.

5. Discussion

The relative Patlak plot is a simplified version of the standard Patlak plot but brings significant advantages for practical use. The theoretical relation between the standard Patlak plot and relative Patlak plot was derived based on the assumption that the tail of a blood input function follows a mono-exponential decay model or meets an approximate linear relation between $x(t)$ and $x'(t)$. This assumption is valid in many dynamic PET scans, as demonstrated in this work by using the popular Feng input model and two blood input functions extracted from real patient data. Even if the tail of a blood input function mathematically follows a more complex model (e.g., a bi-exponential decay model) for accurate description, we have demonstrated that the relation of $x(t)$ versus $x'(t)$ can remain highly linear.

The relative Patlak plot has limitations. Compared with quantitative K_i estimates by the standard Patlak plot, a disadvantage of the relative Patlak plot is that the slope K'_i is not fully quantitative as the information of $s^* = \int_0^* C_P(\tau)dt$ is lost and the global scaling factor cannot be determined. In this regard, we do not recommend the use of K'_i as a replacement for quantitative K_i because the variability in K'_i can be different from patient to patient and from scan to scan. For example, the scaling factor was 1.6199 in the breast cancer patient and1.2898 in the cardiac patient in the patient study. Hence, the relative Patlak plot is not directly suitable for those applications that require absolute quantification of K_i.

However, there are many applications that do not require absolute quantification but utilize the contrast information in the parametric image of K_i. Examples include, but are not limited to, lesion detection (e.g., [Li et al., 2009, Yang et al., 2016]), and metabolic tumor volume segmentation (e.g., [Visser et al., 2008]) using parametric map of tracer influx rate. The target-to-background contrast is often higher in the parametric images than in the SUV images, implying that parametric imaging can offer higher lesion detectability and better boundary differentiation (Fig. 8 and Fig. 10). Texture analysis based on parametric images may also provide new insight into tumor heterogeneity beyond the analysis on SUV images. In addition, for cancer imaging, a background region (e.g., the liver) may be defined to normalize the parametric image of the relative Patlak slope, then the global scaling factor can be removed. The normalized K'_i is quantitatively equal to the normalized K_i and can be used for quantitative monitoring in a longitudinal study. We will investigate the feasibility of normalized K'_i for this purpose in a future patient study.

The investigation and development in this work are also timely because recently whole-body Patlak parametric image reconstruction has become available in commercial PET scanners [Hu et al., 2017]. The new relative Patlak plot can have a clear impact on practical use.

6. Conclusion

We propose a new relative Patlak plot method for analyzing dynamic PET data. The new plot excludes the need for early-time input function and only requires late-time input function data, thus is easier to use than the standard Patlak method. Theoretical analysis, simulation results and real patient data all have demonstrated that parametric imaging by the relative Patlak plot determines the parametric image of the standard Patlak slope up to a global scaling factor. The new relative plot can replace the standard Patlak plot for certain applications where the determination of the global scaling factor is not necessary, such as lesion detection, metabolic volume segmentation, and texture analysis.

Acknowledgments

The authors thank the reviewers for helpful comments. The work is supported in part by NIH under no. R21 HL 131385 and by AHA under no. BGIA 25780046. GW is also supported in part by the UC Davis Comprehensive Cancer Center under NIH grant no. P30 CA093373 and K12 CA138464.

References

Angelis GI, Thielemans K, Tziortzi AC, Turkheimer FE, and Tsoumpas C (2011). Convergence optimization of parametric mlem reconstruction for estimation of patlak plot parameters. Computerized Medical Imaging and Graphics, 35(5):407–416. [PubMed: 21295443]

Choi Y, Hawkins RA, Huang SC, Gambhir SS, Brunken RC, Phelps ME, and Schelbert HR (1991). Parametric images of myocardial metabolic-rate of glucose generated from dynamic cardiac pet and 2- f-18 fluoro-2-deoxy-d-glucose studies. Journal of Nuclear Medicine, 32(4):733–738. [PubMed: 2013815]

Choi Y, Huang SC, Hawkins RA, Kuhle WG, Dahlbom M, Hoh CK, Czernin J, Phelps ME, and Schelbert HR (1993). A simplified method for quantification of myocardial blood-flow using nitrogen-13-ammonia and dynamic pet. Journal of Nuclear Medicine, 34(3):488–497. [PubMed: 8280197]

Feng D, Huang SC, and Wang XM (1993). Models for computer-simulation studies of input functions for tracer kinetic modeling with positron emission tomography. International Journal of Bio-Medical Computing, 32(2):95–110. [PubMed: 8449593]

Gambhir SS, Schwaiger M, Huang SC, Krivokapich J, Schelbert HR, Nienaber CA, and Phelps ME (1989). Simple noninvasive quantification method for measuring myocardial glucose-utilization in humans employing positron emission tomography and f-18 deoxyglucose. Journal of Nuclear Medicine, 30(3):359–366. [PubMed: 2786939]

Gill SS, Patel NK, Hotton GR, O'Sullivan K, McCarter R, Bunnage M, Brooks DJ, Svendsen CN, and Heywood P (2003). Direct brain infusion of glial cell line-derived neurotrophic factor in parkinson disease. Nature Medicine, 9(5):589–595.

Gunn RN, Sargent PA, Bench CJ, Rabiner EA, Osman S, Pike VW, Hume SP, Grasby PM, and Lammertsma AA (1998). Tracer kinetic modeling of the 5-ht1a receptor ligand carbonyl-c-11 way-100635 for pet. Neuroimage, 8(4):426–440. [PubMed: 9811559]

Hackstein N, Bauer J, Hauck EW, Ludwig M, Kramer HJ, and Rau WS (2003). Measuring single-kidney glomerular filtration rate on single-detector helical ct using a two-point patlak plot technique in patients with increased interstitial space. American Journal of Roentgenology, 181(1):147–156. [PubMed: 12818847]

Hackstein N, Wiegand C, Rau WS, and Langheinrich AC (2004). Glomerular filtration rate measured by using triphasic helical ct with a two-point patlak plot technique. Radiology, 230(1):221–226. [PubMed: 14645882]

Hom J, Dankbaar JW, Schneider T, Cheng SC, Bredno J, and Wintermark M (2009). Optimal duration of acquisition for dynamic perfusion ct assessment of blood-brain barrier permeability using the patlak model. American Journal of Neuroradiology, 30(7):1366–1370. [PubMed: 19369610]

Hu J, Panin V, Smith AM, H W, Shah Vijay, Kehren F, and Casey M (2017), Clinical whole body CBM parametric PET with flexible scan modes, Conference Record of IEEE Nuclear Science Symposium and Medical Imaging Conference, 2017.

Karakatsanis NA, Zhou Y, Lodge MA, Casey ME, Wahl RL, Zaidi H, Rahmim A, Generalized whole-body Patlak parametric imaging for enhanced quantification in clinical PET, Physics in Medicine and Biology, 201560(22): 8643–8673. [PubMed: 26509251]

Karakatsanis NA, Casey ME, Lodge MA, Rahmim A, Zaidi H, Whole-body direct 4D parametric PET imaging employing nested generalized Patlak expectation-maximization reconstruction, Physics in Medicine and Biology, 201661(15): 5456–5485. [PubMed: 27383991]

Kordower JH, Emborg ME, Bloch J, Ma SY, Chu YP, Leventhal L, McBride J, Chen EY, Palfi S, Roitberg BZ, Brown WD, Holden JE, Pyzalski R, Taylor MD, Carvey P, Ling ZD, Trono D, Hantraye P, Deglon N, and Aebischer P (2000). Neurodegeneration prevented by lentiviral vector delivery of gdnf in primate models of parkinson's disease. Science, 290(5492):767–773. [PubMed: 11052933]

Li Z, Li Q, Yu X, Conti PS, Leahy RM (2009), Lesion detection in dynamic FDG-PET using matched subspace detection, IEEE Transactions on Medical Imaging, 28(2):230–40. [PubMed: 19188110]

Miles KA, Leggett DAC, and Bennett GAJ (1999). Ct derived patlak images of the human kidney. British Journal of Radiology, 72(854):153–158. [PubMed: 10365065]

Patlak CS and Blasberg RG (1985). Graphical evaluation of blood-to-brain transfer constants from multiple-time uptake data - generalizations. Journal of Cerebral Blood Flow and Metabolism, 5(4): 584–590. [PubMed: 4055928]

Patlak CS, Blasberg RG, and Fenstermacher JD (1983). Graphical evaluation of blood-to-brain transfer constants from multiple-time uptake data. Journal of Cerebral Blood Flow and Metabolism, 3(1): 1–7. [PubMed: 6822610]

Rahmim A, Tang J, Zaidi H (2009). Four-dimensional (4D) image reconstruction strategies in dynamic PET: beyond conventional independent frame reconstruction. Medical Physics, 36(8): 3654–70. [PubMed: 19746799]

Reader AJ and Verhaeghe J (2014). 4D image reconstruction for emission tomography. Physics in Medicine and Biology, 59(22):R371–R418. [PubMed: 25361380]

Schmidt KC and Turkheimer FE (2002). Kinetic modeling in positron emission tomography. Quarterly Journal of Nuclear Medicine, 46(1):70–85. [PubMed: 12072847]

Tang J, Kuwabara H, Fwong D, and Rahmim A (2010). Direct 4d reconstruction of parametric images incorporating anato-functional joint entropy. Physics in Medicine and Biology, 55(15):4261–4272. [PubMed: 20647600]

Tsoumpas C, Turkheimer FE, and Thielemans K (2008). Study of direct and indirect parametric estimation methods of linear models in dynamic positron emission tomography. Medical Physics, 35(4):1299–1309. [PubMed: 18491524]

Visser EP, Philippens MEP, Kienhorst L, Kaanders J, Corstens FHM, de Geus-Oei LF, and Oyen WJG (2008). Comparison of tumor volumes derived from glucose metabolic rate maps and suv maps in dynamic f-18-FDG PET. Journal of Nuclear Medicine, 49(6):892–898. [PubMed: 18483085]

Wang GB, Fu L, and Qi JY (2008). Maximum a posteriori reconstruction of the patlak parametric image from sinograms in dynamic PET. Physics in Medicine and Biology, 53(3):593–604. [PubMed: 18199904]

Wang GB and Qi JY (2013). Direct estimation of kinetic parametric images for dynamic PET. Theranostics, 3(10):802–815. [PubMed: 24396500]

Wu Y, and Carson RE (2002). Noise reduction in the simplified reference tissue model for neuroreceptor functional imaging. Journal of Cerebral Blood Flow & Metabolism, 22(12):1440–52. [PubMed: 12468889]

Yang L, Wang G, Qi J (2016), Theoretical analysis of penalized maximum-likelihood Patlak parametric image reconstruction in dynamic PET for lesion detection, IEEE Transactions on Medical Imaging, 35(4): 947–956. [PubMed: 26625407]

Zhu W, Li Q, Bai B, Conti PS, Leahy RM. (2014). Patlak image estimation from dual time-point list-mode PET data, IEEE Transactions on Medical Imaging, 33(4):913–24. [PubMed: 24710160]

Zhou Y, Sojkova J, Resnick SM, Wong DF (2012), Relative Equilibrium Plot Improves Graphical Analysis and Allows Bias Correction of Standardized Uptake Value Ratio in Quantitative ^{11}C PiB PET Studies, Journal of Nuclear Medicine, 53(4): 622–8. [PubMed: 22414634]

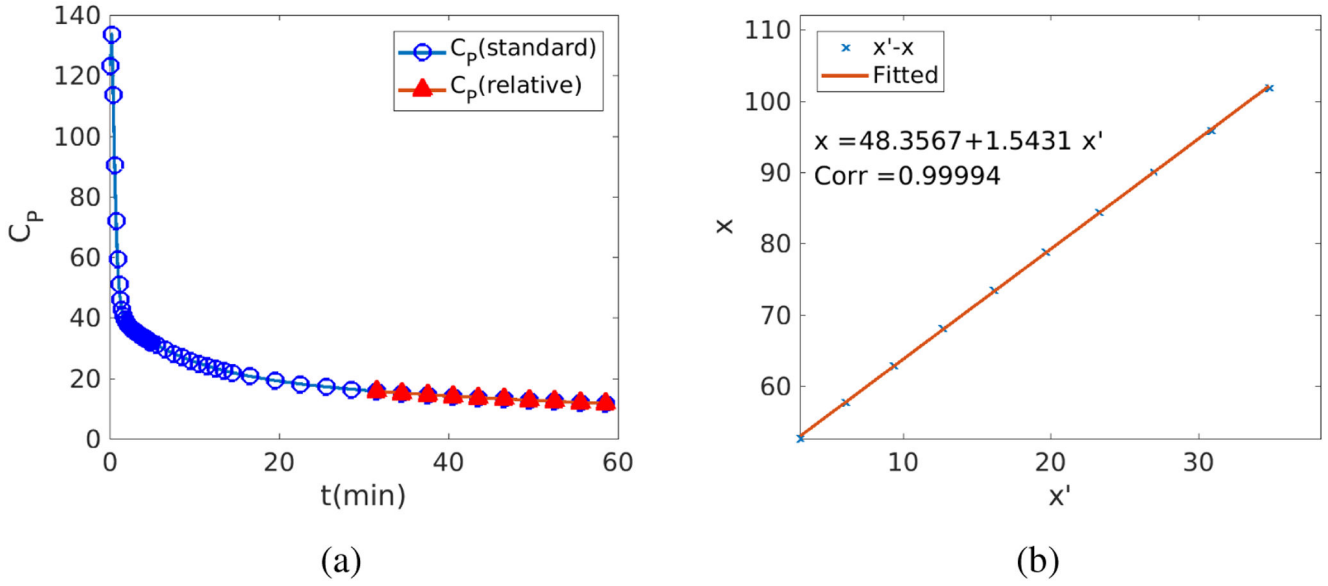

Figure 1.

Blood input functions in the simulation. (a) Full-time blood input function (circles) by the Feng model for the Standard Patlak and late time points (solid triangles) for the relative Patlak; (b) Linear relation between x and x' with t^* = 30 minutes.

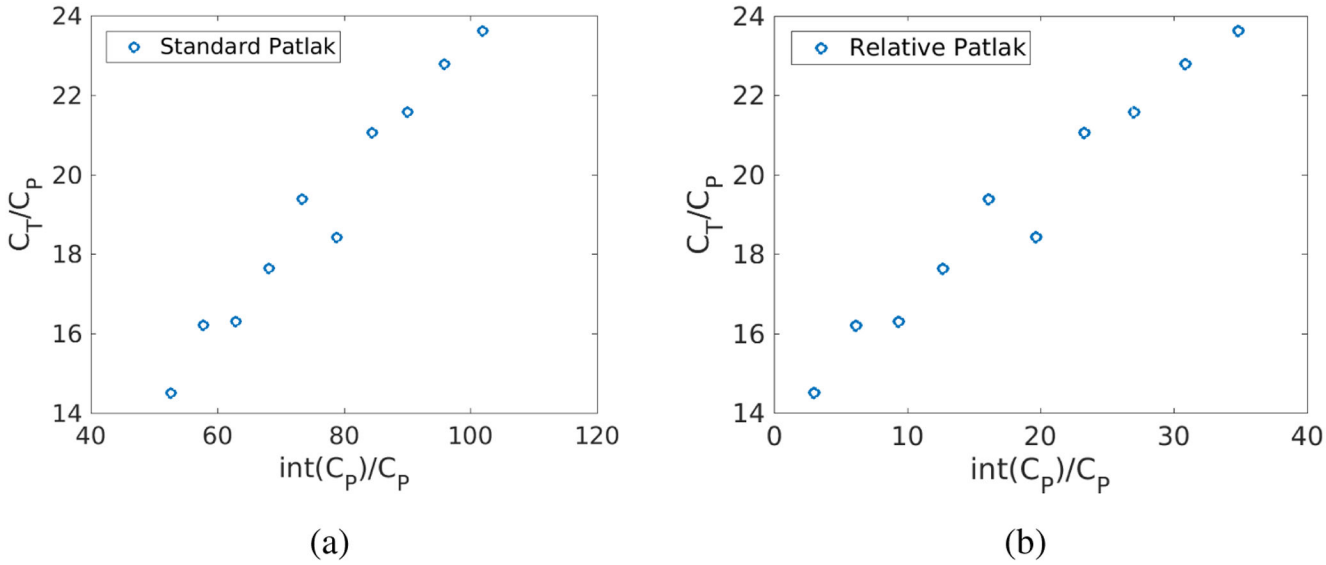

(a) (b)

Figure 2.

Comparison of the standard Patlak plot and relative Patlak plot in the simulation. (a) standard Patlak plot; (b) relative Patlak plot.

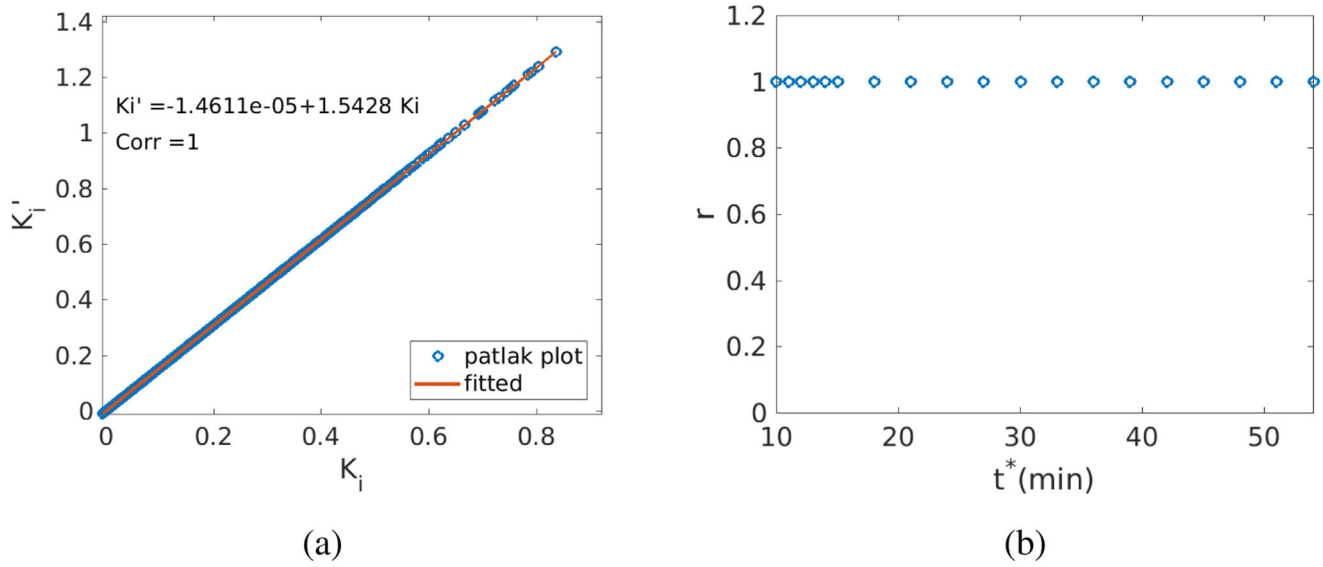

Figure 3.

Results of simulation. (a) Relation between K'_i and K_i; (b) Correlation coefficient of K'_i versus K_i for various t^* values.

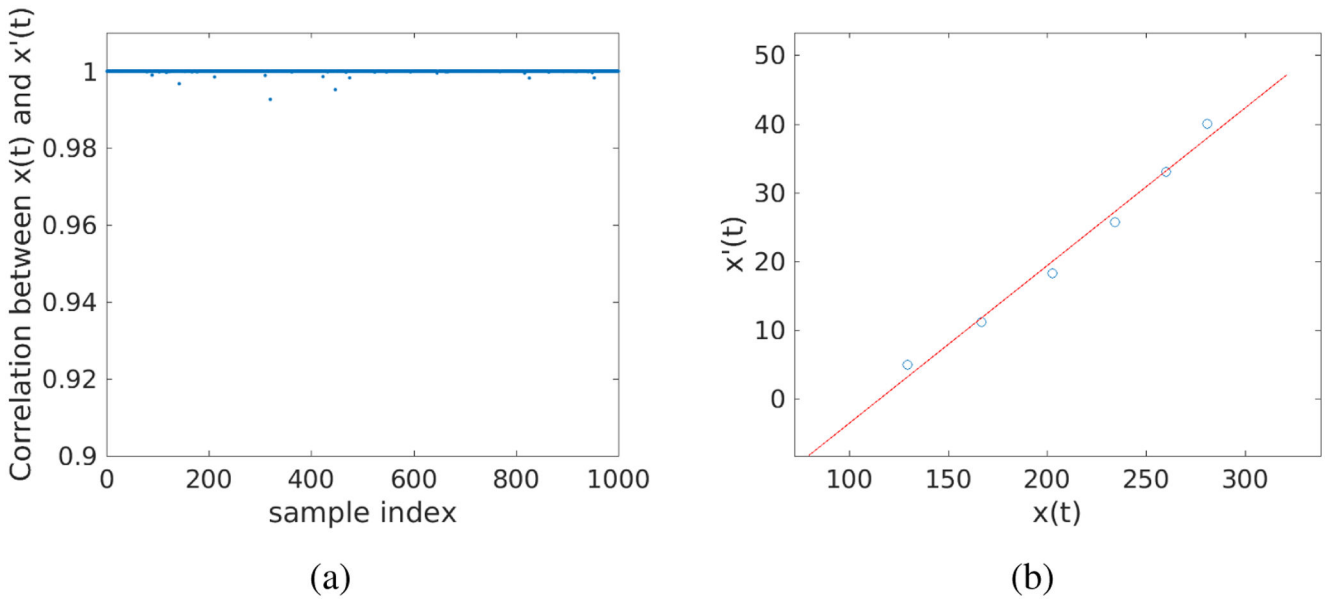

Figure 4.

Validation of the approximate linear relationship between $x(t)$ and $x'(t)$ for the bi-exponential input function $C_P(t) = a_1 e^{-a2t} + b_1 e^{-b2t}$. $t^* = 30$ minutes. (a) Plot of the correlation coefficient of $x(t)$ versus $x'(t)$ for 1,000 realizations; (b) Correlation plot for a specific parameter set that corresponds to the sample point with the lowest correlation coefficient in (a).

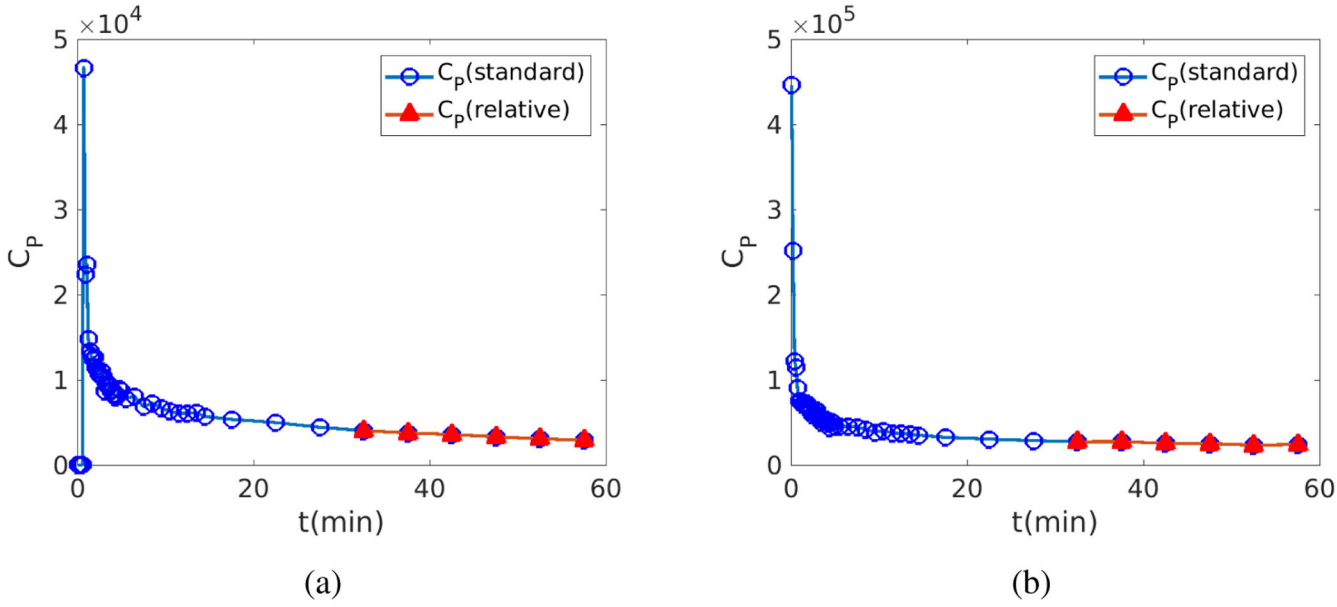

Figure 5.
Blood input functions from dynamic FDG-PET scans of human patients. (a) breast cancer patient; (b) cardiac patient.

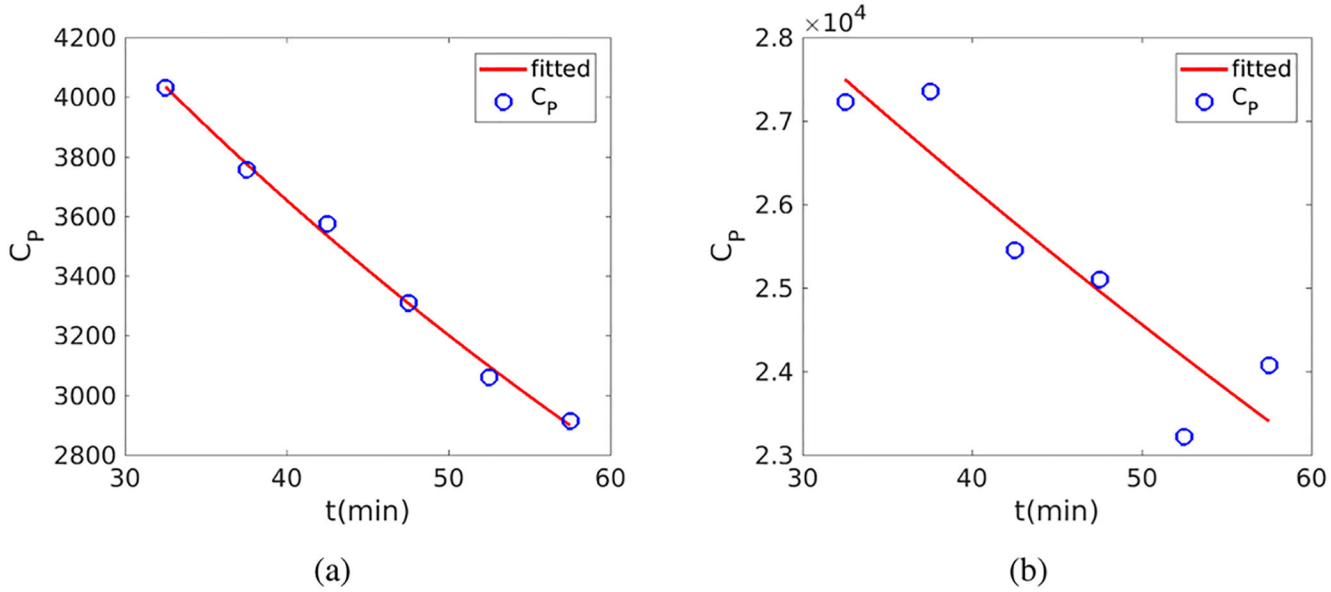

Figure 6.

Validation that late-time points of real patient blood input functions approximately follow a mono-exponential function model. (a) breast patient data, (b) cardiac patient data.

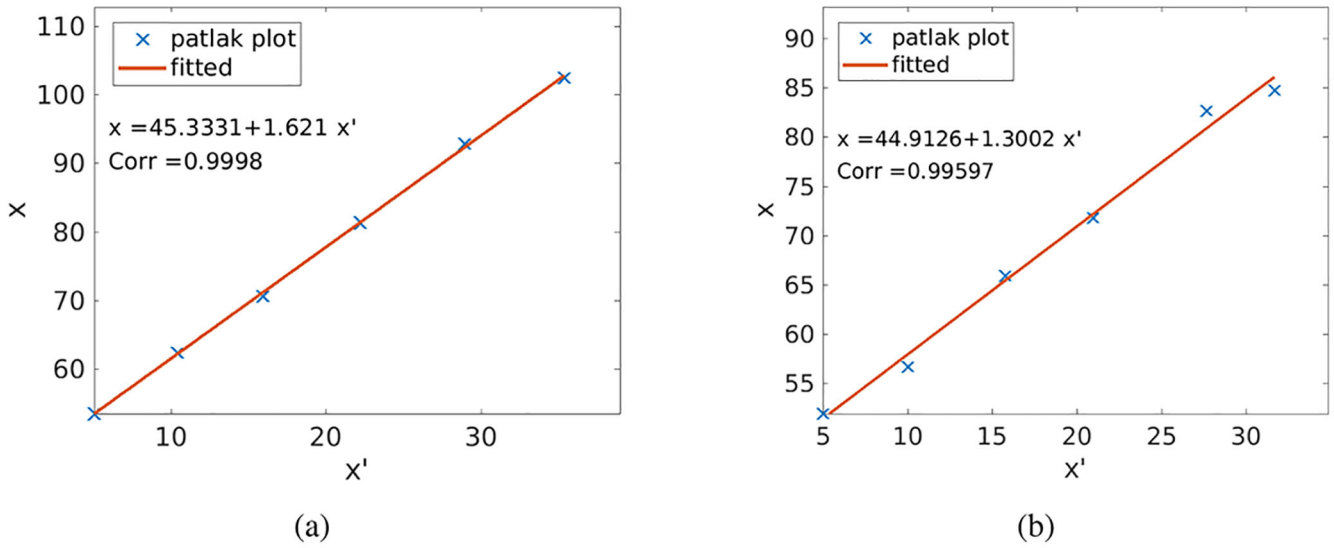

Figure 7.

Linear relation between $x(t)$ and $x'(t)$ for patient data with $t \geq t^* = 30$ minutes.(a) breast patient data, (b) cardiac patient data.

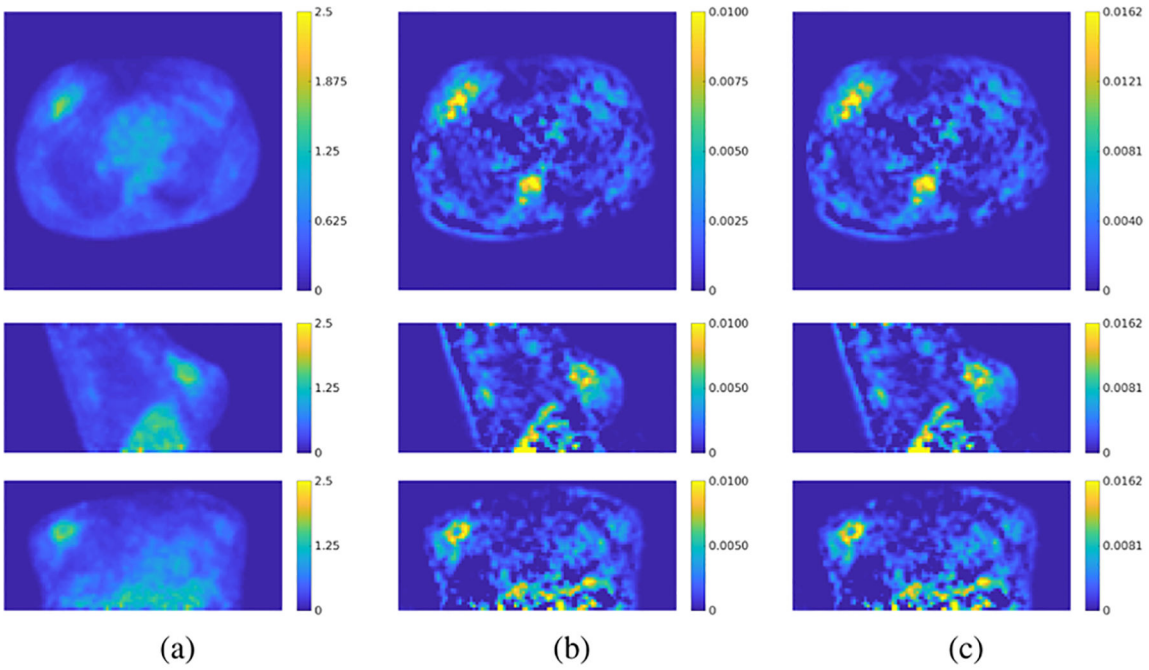

Figure 8.

Comparison of SUV images and parametric imaging using the standard Patlak plot and relative Patlak plot for the breast patient. (a) SUV images; (b) parametric image of the standard Patlak slope K_i; (c) parametric image of the relative Patlak slope K'_i. The start time $t^* = 30$ minutes. From the top to the bottom are the views from the planes of transverse, sagittal and coronal, respectively.

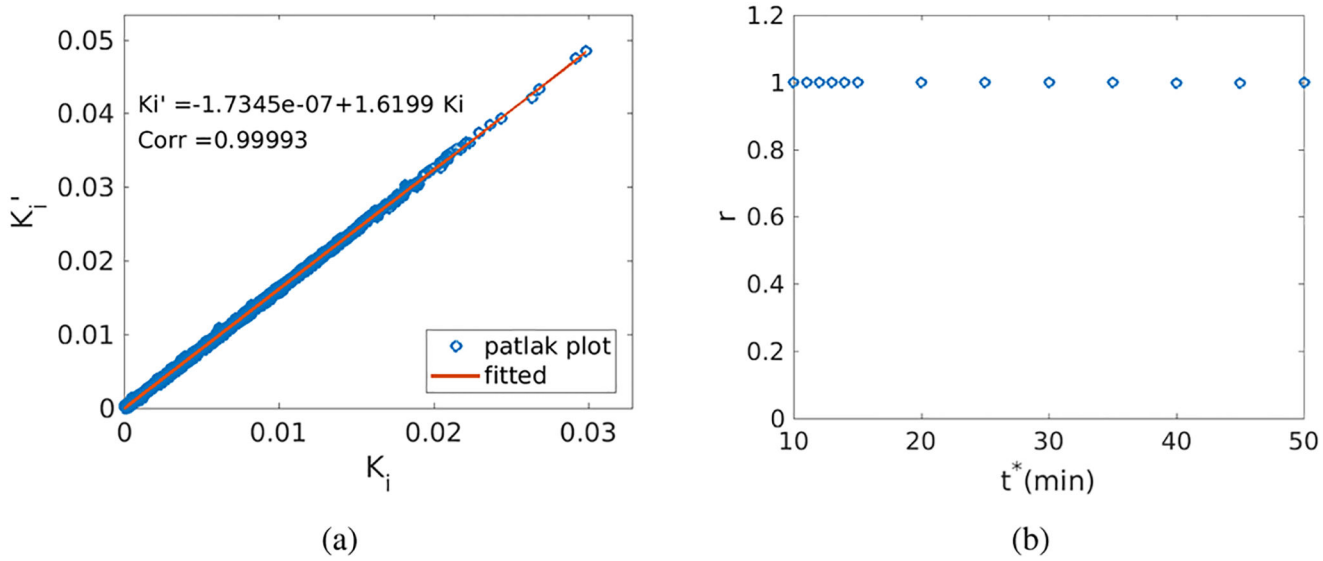

Figure 9.

Results of the breast patient scan. (a) Relation between K'_i and K_i (t^* = 30 minutes); (b) Correlation coefficient between K'_i and K_i versus various start time t^*.

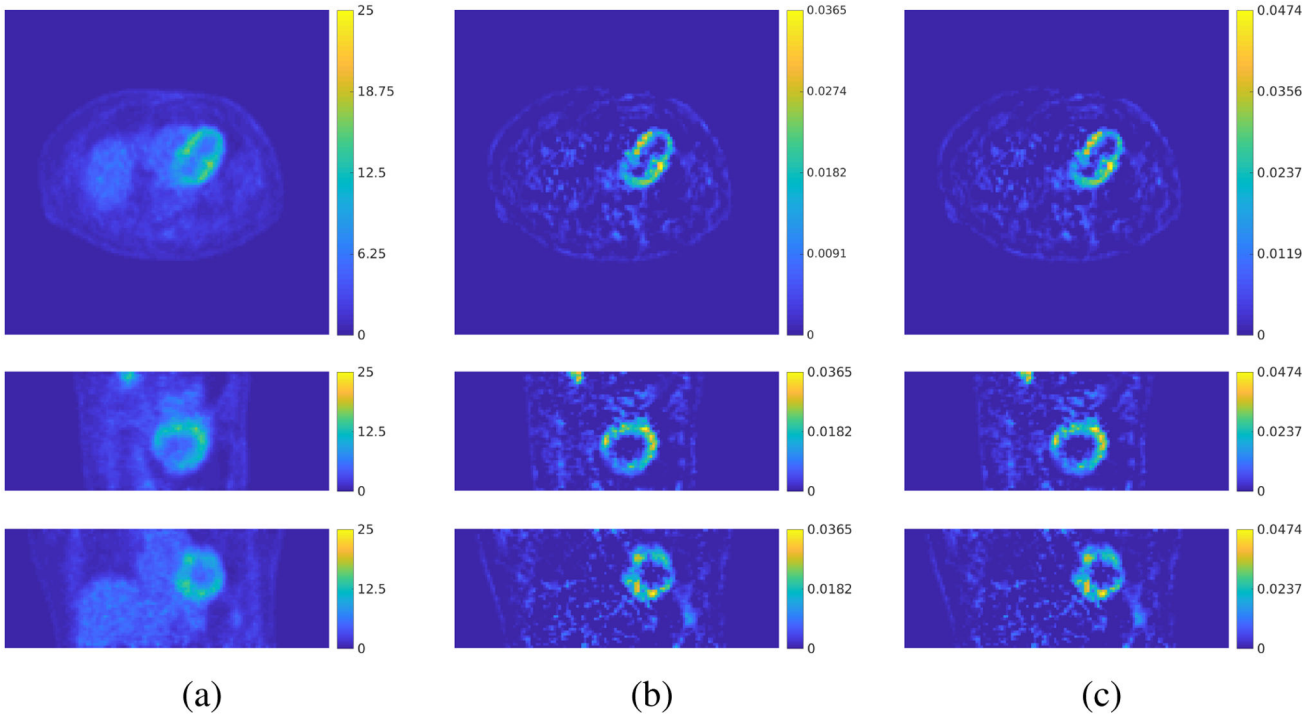

Figure 10.

Comparison of SUV images and parametric imaging using the standard Patlak plot and relative Patlak plot for the cardiac patient. (a) SUV images; (b) parametric image of K_i; (c) parametric image of K'_i. The start time $t^* = 30$ minutes. From the top to the bottom are the views from the planes of transverse, sagittal and coronal, respectively.

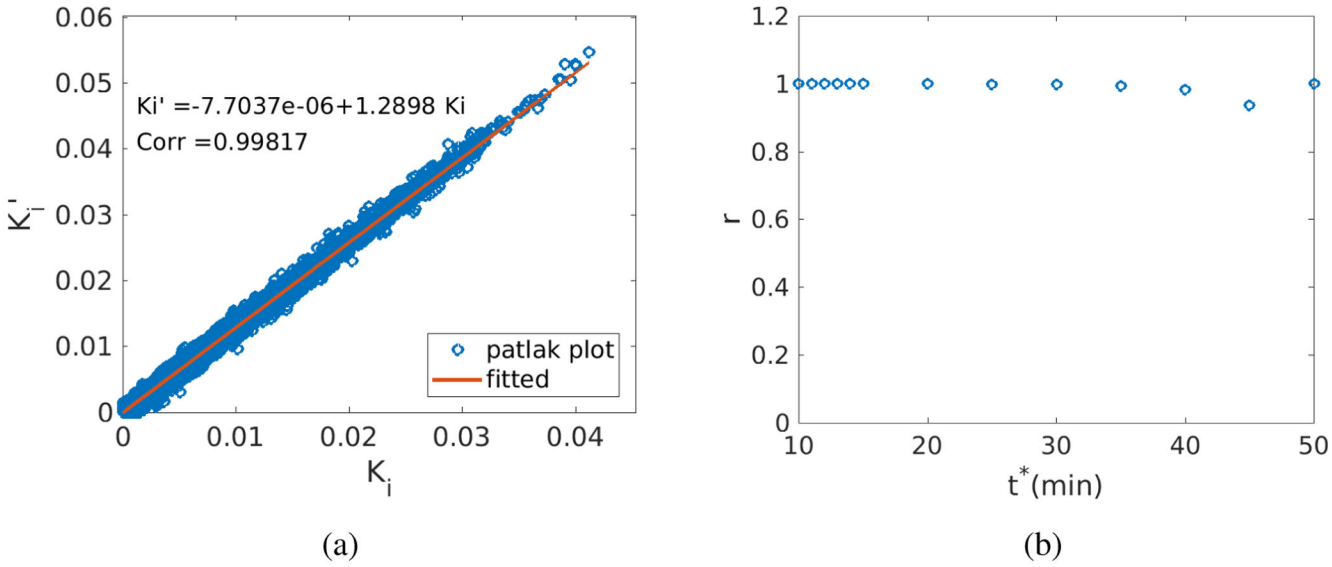

Figure 11.

Results of the cardiac patient scan. (a) Relation between K'_i and K_i (t^* = 30 minutes); (b) Correlation coefficient between K_i and K'_i versus various t^* values.

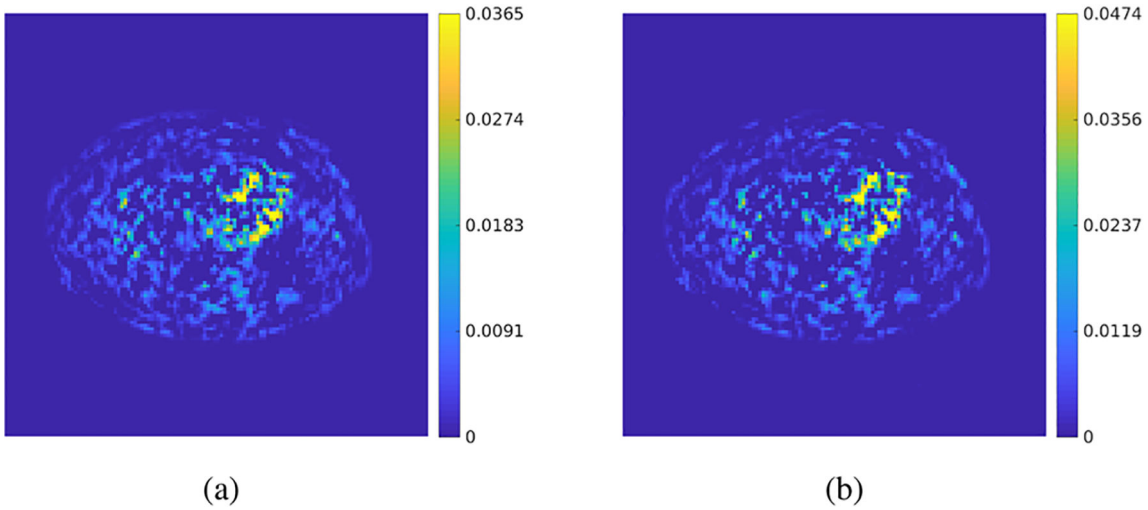

Figure 12.

Parametric images of K_i and K'_i estimated with $t^* = 45$ minutes for the cardiac patient data. (a) K_i by the standard Patlak plot; (b) K'_i by the relative Patlak plot.